

## MATERIALS SCIENCE

# Achieving large uniform tensile elasticity in microfabricated diamond

Chaoqun Dang<sup>1\*</sup>, Jyh-Pin Chou<sup>1,2\*</sup>, Bing Dai<sup>3\*</sup>, Chang-Ti Chou<sup>4\*</sup>, Yang Yang<sup>5</sup>, Rong Fan<sup>1</sup>, Weitong Lin<sup>1</sup>, Fanling Meng<sup>6</sup>, Alice Hu<sup>1,7†</sup>, Jiaqi Zhu<sup>3†</sup>, Jiecai Han<sup>3</sup>, Andrew M. Minor<sup>5</sup>, Ju Li<sup>8†</sup>, Yang Lu<sup>1,7,9†</sup>

Diamond is not only the hardest material in nature, but is also an extreme electronic material with an ultrawide bandgap, exceptional carrier mobilities, and thermal conductivity. Straining diamond can push such extreme figures of merit for device applications. We microfabricated single-crystalline diamond bridge structures with ~1 micrometer length by ~100 nanometer width and achieved sample-wide uniform elastic strains under uniaxial tensile loading along the [100], [101], and [111] directions at room temperature. We also demonstrated deep elastic straining of diamond microbridge arrays. The ultralarge, highly controllable elastic strains can fundamentally change the bulk band structures of diamond, including a substantial calculated bandgap reduction as much as ~2 electron volts. Our demonstration highlights the immense application potential of deep elastic strain engineering for photonics, electronics, and quantum information technologies.

**D**iamond is the “Mount Everest” of electronic and photonic materials (1–3) because of its ultrahigh thermal conductivity (4), dielectric breakdown strength (2), carrier mobility (5), and ultrawide bandgap (6, 7). One serious obstacle to realizing diamond-based electronic and optoelectronic devices is the doping challenge (8–10) caused by the large bandgap and its crystal structure. A potential solution is to apply elastic lattice strain, which can substantially change the material properties (11–13). Ultralarge elastic deformation was recently demonstrated by bending a nanoscale diamond needle. The local tensile elastic strain reached 9% (14) or higher (15) in a region tens of nanometers in size, with the corresponding strength approaching diamond’s theoretical limit (16, 17). This discovery suggests that deep elastic strain engineering (ESE) (18, 19), in which very high (>5%) tensile and/or shear elastic strains are induced in diamond, may

allow for physical properties to be fundamentally changed. However, we require precise control in a large enough volume to fully use deep ESE for very large-scale integration in industry. Past attempts at straining diamond were often limited by the strain being within a small sample volume by flexural bending, resulting in nonuniform strain distribution (14, 15). Those samples are hard to control,

and the resulting high-strain field is highly localized. A large uniform elastic strain over substantial volume is often the desired initial state (18, 20) for deep ESE of an array of devices. This scenario is difficult to realize experimentally in a micrometer-scale sample, for example, in a clean wafer, because of the well-known “smaller is stronger” trend (12), which suggests that increasing size weakens the sample.

We demonstrate extremely large, reversible, and uniform elastic deformation in microfabricated single-crystalline diamond bridges under tensile loading. To produce tensile samples up to ~1-μm length by 300-nm width with well-defined geometry and crystal orientations, we used advanced microfabrication processes of bulk single-crystalline diamonds that were grown through microwave plasma-assisted chemical vapor deposition (21, 22). The process we developed produces high-quality diamond structures with micrometer dimensions, which are prime candidates for microelectromechanical systems (MEMS), quantum and photonic devices, arrays of strain-engineered transistors, and other applications. We used a homemade diamond tensile gripper to uniaxially stretch focused ion beam (FIB)-sculpted diamond from the bulk single crystal (23). We investigated key characteristics of

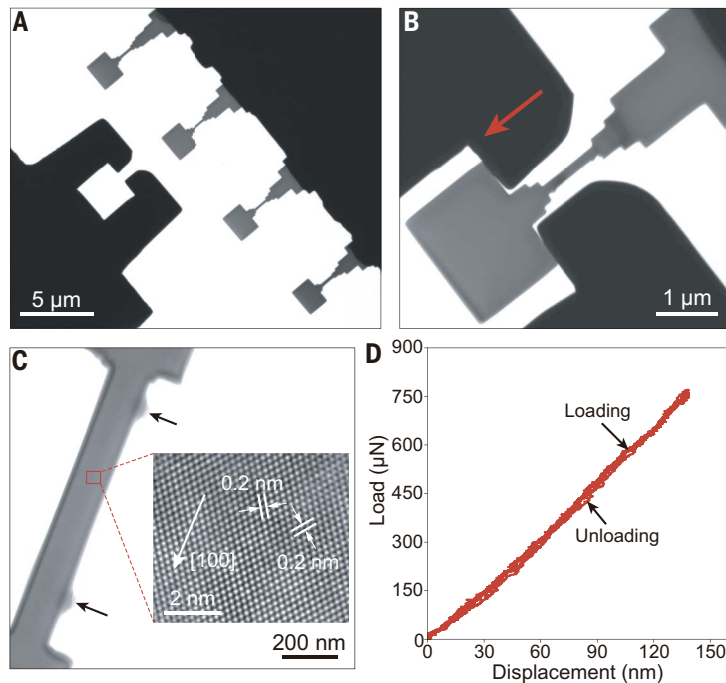


**Fig. 1. Microfabricated single-crystalline diamond bridge samples.** (A) Side-view TEM image showing the microfabricated diamond bridge samples and corresponding diamond tensile gripper. (B) Tensile sample and the diamond gripper aligned before straining. (C) Higher-magnification image depicting the gauge area with two fiducial markers (made by electron-beam-induced carbon deposition, as indicated by the black arrows), serving as “strain gauge” for the following strain measurement. Inset: HRTEM image depicting the atomic-scale structure of a pristine diamond tensile sample. (D) Typical load-versus-displacement curve read from the nanoindenter for a loading-unloading tensile test under the displacement control mode.

<sup>1</sup>Department of Mechanical Engineering, City University of Hong Kong, Kowloon, Hong Kong. <sup>2</sup>Department of Physics, National Changhua University of Education, Changhua 50007, Taiwan. <sup>3</sup>National Key Laboratory of Science and Technology on Advanced Composites in Special Environments, Harbin Institute of Technology, Harbin 150080, China. <sup>4</sup>Department of Materials Science and Engineering, National Chiao Tung University, Hsinchu 30010, Taiwan. <sup>5</sup>National Center for Electron Microscopy, Molecular Foundry, Lawrence Berkeley National Laboratory, and Department of Materials Science and Engineering, University of California, Berkeley, CA 94720, USA. <sup>6</sup>School of Environmental Science and Engineering, Southern University of Science and Technology, Shenzhen 518055, China. <sup>7</sup>Department of Materials Science and Engineering, City University of Hong Kong, Kowloon, Hong Kong. <sup>8</sup>Department of Nuclear Science and Engineering and Department of Materials Science and Engineering, Massachusetts Institute of Technology, Cambridge, MA 02139, USA. <sup>9</sup>Nano-Manufacturing Laboratory (NML), Shenzhen Research Institute of City University of Hong Kong, Shenzhen, 518057, China.

\*These authors contributed equally to this work.

†Corresponding author. Email: alicehu@cityu.edu.hk (A.H.); zhujq@hit.edu.cn (J.Z.); liju@mit.edu (J.L.); yanglu@cityu.edu.hk (Y.L.)

this reversible and uniform elastic deformation through in situ mechanical tensile experiments of the micrometer-sized diamond bridges at room temperature along the [100], [101], and [111] directions. We used density functional theory (DFT) calculations to estimate the electronic-band structure evolution upon the corresponding loading (24).

We used transmission electron microscopy (TEM) to characterize the microfabricated single-crystalline [100]-oriented diamond (25) (Fig. 1). Our low-magnification TEM image (Fig. 1A) shows several diamond tensile samples and the corresponding microfabricated diamond gripper (figs. S1 and S2). We FIB-sculpted the samples from the bulk diamond body (Fig. 1B), allowing the T-shaped sample to be gripped by the shoulders during the tensile test. We used two fiducial markers that we made using electron-beam-induced carbon deposition (Fig. 1C, black arrows) to serve as a “strain gauge.” Our high-resolution TEM (HRTEM) image shows the atomic-scale structure of a pristine diamond microtensile sample (Fig. 1C, inset). The surface of the FIB-sculpted diamond sample was an ~15-nm-thick amorphous carbon layer (fig. S3). This layer is commonly formed during FIB machining of the diamond (15, 17). A typical load-versus-displacement curve (Fig. 1D) that we measured using a quantitative nanoindenter

for a loading-unloading tensile test under the displacement control shows that fully elastic recovery was likely.

We tested >10 diamond samples for each crystallographic orientation inside a TEM (25) and videorecorded the sample evolution during straining. We extracted a series of TEM images (Fig. 2, A to E) from the video (movie S1) of in situ tension of a single-crystalline [101]-oriented diamond. We completed three complete loading-unloading processes with increasing tensile strain amplitude of a diamond bridge with an ~200-nm thickness. The diamond completely recovered its original length after strain values of ~4.8, 6.8, and 7.5% in each of these cycles, respectively. We used finite element method (FEM) simulation (Fig. 2F) to reproduce the experimental setup (front view), which shows that the diamond has a highly uniform elastic strain distribution (~7.5%) in the interior, with a local maximum strain of ~9.1% near the gripping ends. The engineering stress-strain curves of loading-fully unloading tests indicate a nearly linear elastic response (Fig. 2G). The slope of the stress-strain curves gives a Young’s modulus of ~865 GPa, which is slightly lower than the theoretical Young’s modulus of bulk diamond along the [101] direction (~1100 GPa) (26), likely because of the surface amorphous carbon layer and growth imperfections (27).

We conducted a similar experiment for a diamond bridge along the [100] direction (25) (fig. S4 and movie S2).

To illustrate the potential for device applications, we further optimized the sample geometry using the ASTM standard (28) and microfabricated diamond array samples with multiple bridges (fig. S5C). We demonstrated in situ tensile straining of a diamond bridge array (length ~2  $\mu$ m) in a scanning electron microscope (Fig. 2H and fig. S5) and show the loading-unloading process of a three-bridge array with increasing strain amplitude (movie S3). The diamond array completely recovered its original shape after being uniformly strained to ~5.8% (Fig. 2, I and J) and eventually fractured at ~6% (fig. S5E). We used an FEM simulation (Fig. 2K) to confirm the uniform elastic strain distribution (~5.8%) in the diamond array with minor stress concentrations near the gripping area.

We compiled all the experimental data of the tensile strengths of [100]-, [101]-, and [111]-oriented diamond samples and plotted them against their tensile strains (Fig. 3) with their corresponding fracture morphologies (fig. S6) (25). The maximum elastic strains from the fully reversible runs and the failure run strains for each orientation are marked by the hollow and solid symbols, respectively. Loading-unloading experiments confirmed that the

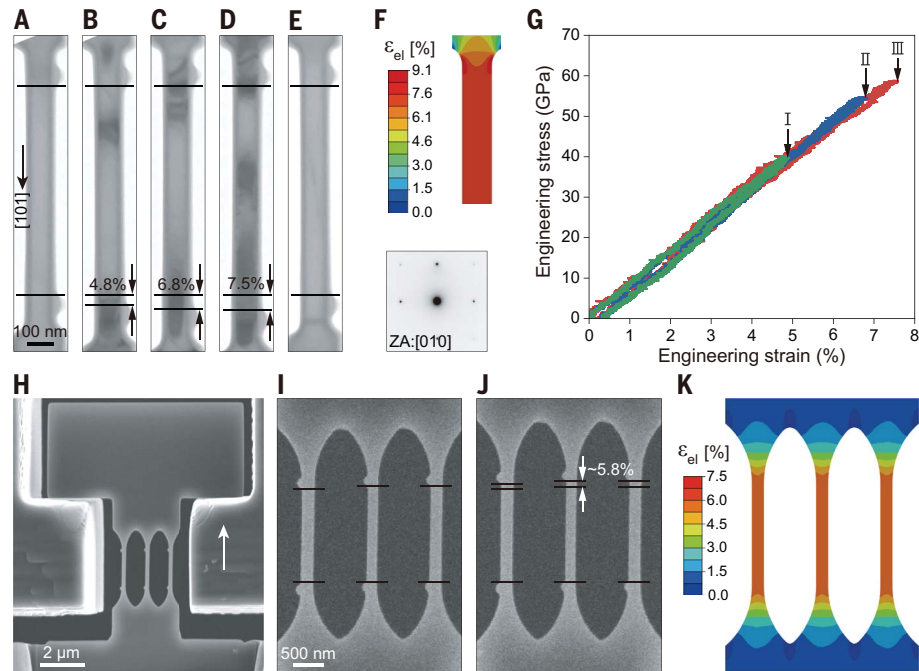


**Fig. 2. Loading-unloading tensile experiments along the [101] direction.** (A to E) Elastic loading-unloading deformation of the diamond bridge sample with increased tensile straining amplitude and full unloading. The diamond recovered its original length after strain values of ~4.8, 6.8, and 7.5% in these cycles. (F) FEM simulation reproducing the critical geometry (front view) of the diamond bridge sample in (D) and showing the elastic strain ( $\epsilon_{el}$ ) distribution along the longitudinal direction. Inset: The [001] zone axis (ZA) selected area electron diffraction pattern depicting that the

loading is parallel to the [101] direction. (G) Corresponding engineering stress-versus-strain curves of multicycle loading-fully unloading tests (I, strain of 4.8%; II, strain of 6.8%; III, strain of 7.5%). (H) Tensile straining of a diamond array sample. (I to J) Elastic loading-unloading deformation of a [101]-oriented diamond array showing maximum 5.8% tensile strain with full recovery. (K) FEM simulation reproducing the critical geometry (front view) of the diamond array sample in (I) shows the highly uniform elastic strain ( $\epsilon_{el}$ ) distribution (~5.8%) along the tensile direction.

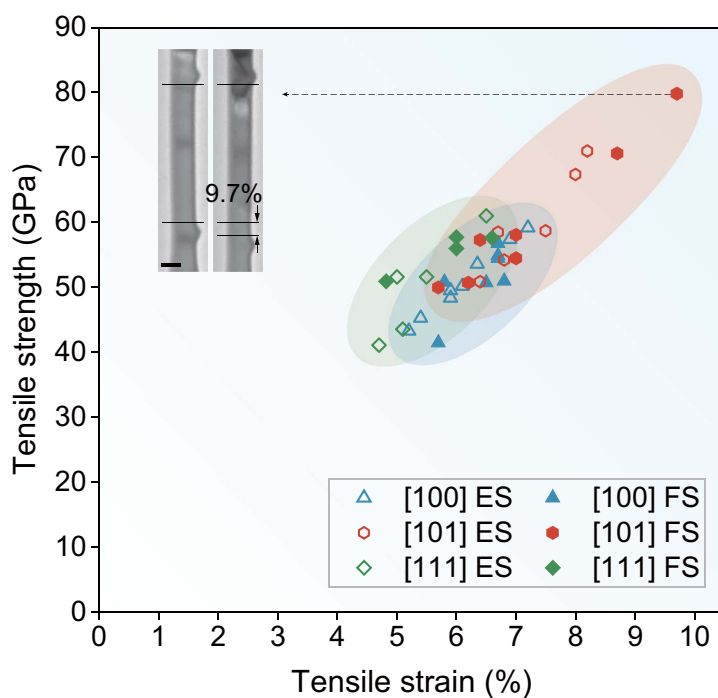


**Fig. 3. Statistical tensile results of [100]-, [101]-, and [111]-oriented diamonds.** Shown is a summary of the engineering tensile strengths of [100]-, [101]-, and [111]-oriented diamond bridge samples versus their tensile strains. The maximum elastic strains (ES) from fully reversible runs and the failure strains (FS) for each orientation are indicated by hollow and solid symbols, respectively. Inset shows a [101]-oriented diamond bridge sample with a maximum tensile strain of ~9.7%. Scale bar, 100 nm.

samples can consistently achieve above 6.5 to 8.2% sample-wide elastic strains with full recovery along the three different orientations. With the optimized sample geometry and microfabrication process, we can achieve maximum tensile strain up to 9.7% (Fig. 3, inset, and fig. S7). This value approaches the ideal elastic limit (16). The Young's modulus we measured is  $\sim 1010 \pm 70$  GPa in the [111] orientation, moderately higher than the values of  $\sim 895 \pm 65$  GPa and  $850 \pm 80$  GPa in the [101] and [100] orientations, respectively. These values are consistent with how the orientation-dependent elastic moduli rank in bulk diamond (26, 27).

As the experiments approach 10% uniform elastic strain, we performed DFT calculations from 0 to 12% strain (figs. S8 to S10 and table S1) to assess the impact on the electronic properties (fig. S11 and movie S4) (25). Generally, the bandgap of diamonds for each direction decreases as the tensile strain increases according to our simulation results. We used an electron energy-loss spectroscopy (EELS) analysis of a strained single-crystalline diamond sample (fig. S12) (25) to verify this trend. The simulation also shows that because the conduction band minimum position switches from the  $\Gamma-X_2$  segment to the  $\Gamma$  point at ~9% strain acting along [111] direction (movie S4), strained diamond becomes a direct-bandgap semiconductor with

a bandgap of ~4.4 eV. Our DFT results indicate that the [101] direction has the largest bandgap reduction rate, down to 3.09 eV at 9% strain.

The fabrication of single-crystalline diamond bridge structures with micrometer-sized dimensions fits well with the scale of MEMS, photonic devices, quantum information processors, and arrays of microelectronic or nanoelectronic devices. The large and uniform elastic strains should drive changes in the bandgap, for which we found evidence using DFT simulation and EELS measurement. Straining along the [101] direction can induce a more substantial bandgap reduction compared with the other two directions. On the basis of our calculations, an indirect-direct bandgap transition may be possible with tensile strains larger than 9% along the [111] direction. These observations are an early step in potentially achieving deep ESE by microfabrication of the free-suspension array configurations and dynamic, reversible mechanical loading for diamond electronic, photonic, and quantum systems (29–31).

#### REFERENCES AND NOTES

- P. W. May, *Science* **319**, 1490–1491 (2008).
- C. J. H. Wort, R. S. Balmer, *Mater. Today* **11**, 22–28 (2008).
- I. Aharonovich, A. D. Greentree, S. Prawer, *Nat. Photonics* **5**, 397–405 (2011).
- J. E. Field, *The Properties of Natural and Synthetic Diamond* (Academic, 1992).
- J. Isberg et al., *Science* **297**, 1670–1672 (2002).
- H. Watanabe, C. E. Nebel, S. Shikata, *Science* **324**, 1425–1428 (2009).
- J. Y. Tsao et al., *Adv. Electron. Mater.* **4**, 1600501 (2018).
- K. Okano, S. Koizumi, S. R. P. Silva, G. A. J. Amaralunga, *Nature* **381**, 140–141 (1996).
- R. Kalish, *Diam. Relat. Mater.* **10**, 1749–1755 (2001).
- Z. Teukam et al., *Nat. Mater.* **2**, 482–486 (2003).
- J. J. Gilman, *Electronic Basis of the Strength of Materials* (Cambridge Univ. Press, 2003).
- T. Zhu, J. Li, *Prog. Mater. Sci.* **55**, 710–757 (2010).
- J. Li, Z. Shan, E. Ma, *MRS Bull.* **39**, 108–114 (2014).
- A. Banerjee et al., *Science* **360**, 300–302 (2018).
- A. Nie et al., *Nat. Commun.* **10**, 5533 (2019).
- D. Roundy, M. L. Cohen, *Phys. Rev. B* **64**, 212103 (2001).
- J. M. Wheeler et al., *Nano Lett.* **16**, 812–816 (2016).
- Z. Shi et al., *Proc. Natl. Acad. Sci. U.S.A.* **116**, 4117–4122 (2019).
- C. Liu, X. Song, Q. Li, Y. Ma, C. Chen, *Phys. Rev. Lett.* **123**, 195504 (2019).
- H. Zhang et al., *Sci. Adv.* **2**, e1501382 (2016).
- G. Shu et al., *CrystEngComm* **20**, 198–203 (2018).
- G. Shu et al., *J. Cryst. Growth* **486**, 104–110 (2018).
- D. Kienzler, A. M. Minor, *Nano Lett.* **11**, 3816–3820 (2011).
- W. Kohn, L. J. Sham, *Phys. Rev.* **140** (4A), A1133–A1138 (1965).
- Materials and methods are available as supplementary materials.
- R. H. Telling, C. J. Pickard, M. C. Payne, J. E. Field, *Phys. Rev. Lett.* **84**, 5160–5163 (2000).
- J. E. Field, *Rep. Prog. Phys.* **75**, 126505 (2012).
- ASTM Standard C1273-18. (ASTM International, 2018); <https://doi.org/10.1520/C1273-18>.
- P. Ovarchayapong, K. W. Lee, B. A. Myers, A. C. B. Jayich, *Nat. Commun.* **5**, 4429 (2014).
- B. Khanaliloo et al., *Phys. Rev. X* **5**, 041051 (2015).
- J. J. Hamlin, B. B. Zhou, *Science* **366**, 1312–1313 (2019).

#### ACKNOWLEDGMENTS

This work was supported by the Research Grants Council of the Hong Kong Special Administrative Region, China, under project no. CityU11207416 and by the National Natural Science Foundation of China under project no. 11922215. J.Z. and B.D. are grateful for financial support from the National Science Fund for Distinguished Young Scholars (grant no. 51625201) and the National Natural Science Foundation of China (grant no. 51702066). A.H. acknowledges funding support from the City University of Hong Kong under project no. 9610336. Y.Y. and A.M.M. acknowledge support from the U.S. Department of Energy, Office of Science, Basic Energy Sciences, Materials Sciences and Engineering Division under contract no. DE-AC02-05-CH11231 to the Mechanical Behavior of Materials Program (KC13) at the Lawrence Berkeley National Laboratory (LBNL). Work at the Molecular Foundry was supported by the Office of Science, Office of Basic Energy Sciences, U.S. Department of Energy under contract no. DE-AC02-05CH11231. J.L. acknowledges support from Office of Naval Research MURI grant no. N00014-17-1-2661. **Author contributions:** Y.L. conceived the research. Y.L., A.H., J.Z., and J.L. supervised the research. C.D., J.-P.C., B.D., C.-T.C., Y.Y., and R.F. performed the research. C.D., J.-P.C., B.D., C.-T.C., Y.Y., R.F., W.L., A.M.M., J.L., and Y.L. analyzed the data. C.D., J.-P.C., B.D., C.-T.C., Y.Y., R.F., J.L., and Y.L. wrote the manuscript. All authors discussed the results and contributed to the final manuscript. **Competing interests:** The authors declare no competing financial interests. **Data and materials availability:** All data are reported in the paper or the supplementary materials.

#### SUPPLEMENTARY MATERIALS

[science.sciencemag.org/content/371/6524/76/suppl/DC1](https://science.sciencemag.org/content/371/6524/76/suppl/DC1)

Materials and Methods

Supplementary Text

Figs. S1 to S12

Table S1

References (32–47)

Movies S1 to S4

29 April 2020; accepted 23 November 2020  
10.1126/science.abc4174

## Achieving large uniform tensile elasticity in microfabricated diamond

Chaoqun Dang, Jyh-Pin Chou, Bing Dai, Chang-Ti Chou, Yang Yang, Rong Fan, Weitong Lin, Fanling Meng, Alice Hu, Jiaqi Zhu, Jiecai Han, Andrew M. Minor, Ju Li and Yang Lu

Science 371 (6524), 76-78.  
DOI: 10.1126/science.abc4174

### Stretching diamond to the limit

Diamond is thought of as being unbendable, but thin samples can actually deform elastically. Applying relatively large amounts of strain to diamond may shift its electronic properties, which is of interest for a number of applications. Dang *et al.* elastically stretched micrometer-sized plates of diamond along different crystallographic directions. These relatively large samples show that deep-strain engineering can be accomplished in more uniform diamond specimens and may have a large impact on the electronic properties.

Science, this issue p. 76

#### ARTICLE TOOLS

<http://science.scienmag.org/content/371/6524/76>

#### SUPPLEMENTARY MATERIALS

<http://science.scienmag.org/content/suppl/2020/12/29/371.6524.76.DC1>

#### REFERENCES

This article cites 45 articles, 8 of which you can access for free  
<http://science.scienmag.org/content/371/6524/76#BIBL>

#### PERMISSIONS

<http://www.scienmag.org/help/reprints-and-permissions>

Use of this article is subject to the [Terms of Service](#)

## Supplementary Materials for

### Achieving large uniform tensile elasticity in microfabricated diamond

Chaoqun Dang\*, Jyh-Pin Chou\*, Bing Dai\*, Chang-Ti Chou\*, Yang Yang, Rong Fan, Weitong Lin, Fanling Meng, Alice Hu†, Jiaqi Zhu†, Jiecai Han, Andrew M. Minor, Ju Li†, Yang Lu†

\*These authors contributed equally to this work.

†Corresponding author. Email: [alicehu@cityu.edu.hk](mailto:alicehu@cityu.edu.hk) (A.H.); [zhujq@hit.edu.cn](mailto:zhujq@hit.edu.cn) (J.Z.);  
[liju@mit.edu](mailto:liju@mit.edu) (J.L.); [yanglu@cityu.edu.hk](mailto:yanglu@cityu.edu.hk) (Y.L.)

Published 1 January 2021, *Science* **371**, 76 (2020)  
DOI: [10.1126/science.abc1474](https://doi.org/10.1126/science.abc1474)

#### This PDF file includes:

- Materials and Methods
- Supplementary Text
- Figs. S1 to S12
- Table S1
- Captions for Movies S1 to S4
- References

#### Other Supplementary Material for this manuscript includes the following: (available at [science.scienccemag.org/content/371/6524/76/suppl/DC1](https://science.scienccemag.org/content/371/6524/76/suppl/DC1))

- Movies S1 to S4 (mp4)

## Materials and Methods

### Microfabrication of the diamond bridge samples

Single-crystalline diamonds (about 5 mm × 5 mm × 1-2 mm) of [100], [101] and [111] orientations were produced by the microwave plasma-assisted chemical vapor deposition growth (21, 22). We microfabricated the diamond tensile samples by using FIB (FEI Scios<sup>TM</sup> DualBeam<sup>TM</sup>) machining of the three-oriented facets. Gallium ion beam currents from 15 nA to 1.5 pA under an operating voltage of 30 kV were used from the initial sculpting to final thinning, respectively. Firstly, a thin lamella was milled from a single-crystalline bulk diamond (Fig. S1A) by using FIB with selective deposition of a platinum (Pt) protection layer on the top (Fig. S1B). Then, the lamella was cut and transferred (Fig. S1C and D) onto a TEM half-grid (Fig. S1E and F) fixed by Pt welding. The lamella was then cut into 6 individual specimens (Fig. S1G), with further thinning processes monitored by top-view imaging (Fig. S1H). Finally, the individual specimens were consequently sculpted into T-shaped bridge tensile samples (Fig. S1I and Fig. S2A and B). The corresponding diamond gripper was sculpted from a solid diamond indenter tip, as shown in Fig. S2C and D. The final diamond bridge samples have effective sizes with widths (and thicknesses) of ~100-300 nm and length of ~1 μm, determined from the top-view and side-view SEM and TEM images, respectively.

### in situ Tensile testing

Quantitative tensile tests were performed with a Hysitron<sup>TM</sup> PI 95 TEM PicoIndenter holder, an in situ mechanical deformation instrument that enables the deformation process to be observed in a TEM (JEOL<sup>TM</sup> JEM-2100F) operating at 200 kV. The nominal strain rate was about  $2.5 \times 10^{-3}$  s<sup>-1</sup> under displacement control. in situ Tensile tests were also conducted inside an SEM (FEI Quanta<sup>TM</sup> 450FEG) operating at 10 kV, by using a Hysitron<sup>TM</sup> PI 85 PicoIndenter.

### FEM analyses

The stress and strain distributions of diamond bridge samples during tensile testing were evaluated with three-dimensional (3D) FEM simulation of the diamond samples subject to uniaxial tension. We carried out the simulation using the commercial ABAQUS (Dassault Systèmes Simulia Corp., Providence, RI, U.S.A.) software package following the actual 3D geometry for each microfabricated sample. The axial displacement control was imposed to the end of the diamond while the traction along the transverse direction was kept free. To take into account the nonlinear elastic deformation beyond about 2%, the neo-Hookean nonlinear elasticity model was used in the simulations, with the material parameters  $C_{10} = 245$  GPa,  $D_1 = 4.91 \times 10^{-3}$  GPa<sup>-1</sup> for [100]-oriented diamonds, and  $C_{10} = 272$  GPa,  $D_1 = 4.43 \times 10^{-3}$  GPa<sup>-1</sup> for [101]-oriented diamonds, respectively (32). The equivalent small strain linear elasticity parameters are: Young's modulus  $E = 1050$  GPa (along [100]) and 1165 GPa (along [101]), respectively, with Poisson's ratio  $\nu = 0.07$  (26). The maximum principal stress state prior to fracture for each diamond case can also be obtained. We validate the accuracy of the simulations by comparing the simulation results to the results of the actual in situ experiments.

### DFT calculation for electronic properties

To illustrate the changes and variations of the electronic structure under such large elastic strains along with different directions, we performed first-principles calculations for the strains from 0 to 12% with an interval of 1%, and the results are summarized in Fig. S11. The first-principles calculations are based on density functional theory (DFT), as implemented in Vienna *ab*

*initio* simulation package (VASP) (33, 34) with projector augmented wave (PAW) (35) method and a plane wave basis set. Unlike previous calculation studies (18, 36), we conduct simulations based on our experiment configuration and sample orientations. The Perdew-Burke-Ernzerhof (PBE) (37) form of the generalized gradient approximation functional is adopted to describe the exchange-correlation energy. We use PBE functional for structural optimization and introduce meta-GGA Made Simple 0 (MGGA-MS0) (38, 39) functional to obtain accurate electronic structures. The energy cutoff for the plane wave expansion is 450 eV and k-point sampling is  $8 \times 8 \times 8$  for diamond primitive cell calculation, which leads to good convergence. The energy threshold is  $10^{-5}$  eV. The optimized lattice constant of the diamond is 3.57 Å. For band structure calculation, the k-points we used in the Brillouin zone (BZ) are shown in Fig. S8 and Table S1. We performed the Poisson contraction relaxation and internal coordinate optimization for each strain. The results and the corresponding bandgap values are shown in Fig. S9. The energy variations are tiny, reflecting small Poisson's ratio, which is consistent with experimental observations (40).

#### Characterization of bandgap by monochromated EELS

EELS spectrums including low loss and core loss were collected from a pre-strained diamond sample using TEAM 1 scanning transmission electron microscope (STEM) at National Center for Electron Microscopy, Lawrence Berkeley National Laboratory, working at 300 kV. The microscope is double aberration-corrected and monochromated with an energy resolution of 0.15 eV (measured by the full-width at half-maximum of the zero-loss peak). A Gatan™ K3 camera with GIF continuum was used to collect the EELS signal at high efficiency. The convergence angle and collection angle were set to be 20 mrad and 27.1 mrad, respectively. After data collection, EELS data were analyzed and processed with Gatan™ Digital Micrograph software, following the procedures in the publication of Hirai *et al.* (41). Firstly, we removed the Plural scattering by the Fourier-Log method with the default reflected tail zero-loss model. Then we performed Kramers-Kronig Analysis (KKA) to obtain plots of the imaginary part of the dielectric function ( $\varepsilon_2$ ) as a function of energy loss, where the onset position of  $\varepsilon_2$  corresponds to the bandgap of the material.

#### **Supplementary Text**

##### Additional experiment on a single-crystalline [100]-oriented diamond sample

Fig. S4 shows *in situ* monotonic tensile test of an [100]-oriented diamond bridge sample. A series of TEM images (Fig. S4A and B) extracted from Movie S2 show the diamond bridge at the original state and the maximum deformation state before fracture. The diamond fractured outside the section between the two markers at a strain of 6.8% and then recovered its original gauge length, as shown in Fig. S4C, suggesting elastic deformation. The diamond has a typical {111} cleavage fracture morphology, and the fractured diamond retains its pristine single-crystalline structure determined by the SAED pattern (Fig. S4D). The distribution of maximum principal stress before the fracture from FEM is shown in Fig. S4D, which reveals the almost sample-wide uniform stress distribution. Slight local stress concentration still shows near the gripping area, resulting in the fracture often initiating near the gripping area and forming {111}-facets cleavage.

##### Fracture morphologies of diamond bridge samples upon tensile fracture

Typical fracture morphologies of diamond bridges along [100], [101] and [111] directions are shown in Fig. S6. They have typical brittle fracture morphologies with no visible sign of plasticity or amorphization (42, 43) during tensile deformation, in which the fractured bridges retain the

pristine single-crystalline structure determined by the inserted SAED patterns (Fig. S6A, B, and C). The fractured parts show typical distinct {111} cleavage surfaces, which are known to have the lowest surface energy and typically observed during brittle fracture of bulk diamonds (4, 26, 27).

#### Confirmation of conduction band minimum (CBM) positions

To confirm the CBMs shown in Fig. S11 are globally the lowest conduction band in the Brillouin zone, we performed density of state (DOS) calculations using highly dense k-point sampling of  $32 \times 32 \times 32$ . The DOS calculations results are consistent with the band structure results. We then further performed band structure calculations along symmetric X points in the whole Brillouin zone, as shown in Fig. S10A. The ideal diamond has a geometric symmetry of  $O_h$ , and is reduced to  $D_{4h}$ ,  $D_{2h}$  and  $D_{3d}$  while a strain applied along [100], [101], and [111] directions, respectively. As shown in Fig. S10B, the band structure of the ideal diamond reveals six-fold degeneracy of CBMs on the regions between  $\Gamma$  and the six symmetric points of X, *i.e.*,  $X_1$ - $X_6$ . The degeneracy of CBMs reduced as the strain applied. As one can see in Fig. S10C to E, the degeneracies of CBMs are split into four-fold for [100]-oriented strained diamond and two-fold for [101]-oriented strained diamonds, but it keeps six-fold for [111]-oriented strained case.

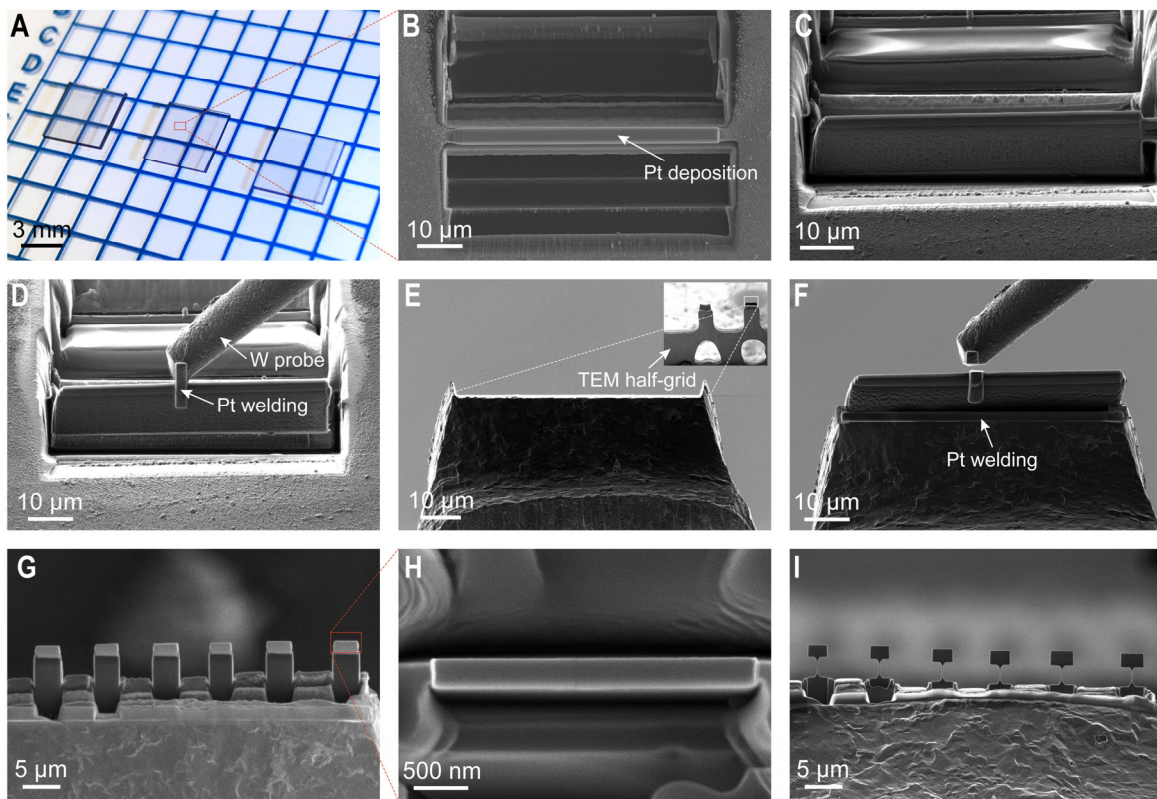
#### Band structure evolution for strained diamond along with different directions

Fig. S11A shows the band structure of the stress-free diamond: the valence band maximum (VBM) appears at  $\Gamma$  point (orange dot), while CBMs appear on  $\Gamma$ -X segments (red dot) with 6-fold degeneracy ( $\pm X_1$ ,  $\pm X_2$ ,  $\pm X_3$  are parallel to  $2\pi/a[100]$ ,  $2\pi/a[010]$  and  $2\pi/a[001]$  in reciprocal space, respectively, where  $a$  is the lattice constant). With [100]-, [101]- and [111]-oriented tensions, the crystal loses its original cubic symmetry, and so the 6 X-points in the Brillouin zone are no longer all equivalent like in the cubic case. We have traced all k-points and found a k-point along  $\Gamma$ - $X_2$  segment, corresponding to  $k_y$  direction in the reciprocal space, remains the CBM with 4-fold, 2-fold and 6-fold energy degeneracy for [100]-, [101]- and [111]-tension, respectively. The segments  $\Gamma$ -( $\pm X_1$ ,  $\pm X_2$ ,  $\pm X_3$ ) are plotted in Fig. S8 and Fig. S10 to show the symmetry breaking. These CBM assignments have been verified by full-BZ density-of-states calculation as discussed above (Fig. S10). Fig. S11B to D display the band structures for various [100]-, [101]- and [111]-uniaxial tensile strains, respectively, which are also illustrated in Movie S4. Five lines with different color shades represent uniaxial strains of 0%, 3%, 6%, 9% and 12% (without Poisson contraction as considered in Fig. S9), of which the darker color stands for larger strain. These results indicate that the VBMs generally stay at  $\Gamma$  point, but the CBMs drift to different positions during straining, thus optical absorption would require quite different phonon momentum assistance with deep straining. For uniaxial straining of diamond in [100] direction, as shown in Fig. S11B, the CBMs retain on  $\Gamma$ - $X_2$  segment and drop in energy with increasing strain. For the strains along [101] direction, as shown in Fig. S11C, the doubly degenerate conduction band around X point splits into two individual bands when strain is applied. As the strain increases, the CBM moves and reaches  $X_2$  point when the strain is larger than 6%. For the strains acting along [111] direction (Fig. S11D), interestingly, the conduction bands on  $\Gamma$ - $X_2$ -U segment have behavior like [101] tension, but the conduction bands at  $\Gamma$  points drop more rapidly than that on  $\Gamma$ - $X_2$ -U segment. Eventually, the CBM position switches to  $\Gamma$  point at ~9% strain, which means that it becomes a direct bandgap semiconductor (Movie S4) with a bandgap of ~4.4 eV. The relationship between strain and bandgap value is summarized in Fig. S11E. The relationship for [100]-straining appears linear, and interestingly, the CBM positions do not shift much with strain.

For [101]-straining, a moderately linear evolution can be observed, attributed to CBM gradually sliding from its original position to X point and then staying there above 6% strain. In contrast, the [111] curve shows more complicated behavior. It decreases parabolically before the strain reaches 9%, that CBM varies only in the  $\Gamma$ -X<sub>2</sub> segment, and later it turns straight because of CBM drifting to  $\Gamma$  point, driving the indirect-direct bandgap transition.

#### Characterization of bandgap of diamond by monochromated EELS

To experimentally verify that the bandgap of diamond can be tuned by applying elastic strain, we have performed monochromatic EELS characterization of a pre-strained single-crystalline diamond sample. Fig. S12A shows the schematic diagram of the pre-strained diamond sample. A bent T-shaped diamond with a crack in the middle was shown in Fig. S12B and C, and EELS low loss signals are collected at three different sample regions (a, b, and c). By finite element modeling and analytical solution (44), the elastic strain field can be estimated and confirmed the positive stress state near the crack tip area. Also, the region (c) closer to the crack tip should have a higher strain than the region (b), while the region in (a) would have little or no strain, showing the intrinsic diamond bandgap value as the reference. We also collected the core loss spectrum corresponding to the regions (b) and (c), which confirms that these regions are still in typical CVD crystalline diamond structure because the characteristic peaks of inset shown in Fig. S12C matched well with that reported in the work of Blake *et al.* (45). It was found that overall the measured bandgap values (Fig. S12D) in regions (a), (b) and (c) agree well with their respective local strain states, *i.e.*, the bandgap energy ( $E_g$ ) is lower when the local tensile strain is higher. Despite that the accuracy of bandgap measured by EELS might be affected by many factors (46, 47), such as multiple scattering and retardation effect, the trend of decreasing  $E_g$  from the local areas with little/no strain to high strain (a to c) is clearly shown, agreeing with the trend in our DFT calculations (Fig. S11).



**Fig. S1.**

**Microfabrication process of the diamond bridge samples.** (A) Optical image of single-crystalline bulk diamond samples. (B and C) A thin lamella was milled using FIB with selective deposition of a platinum (Pt) protection layer on the top. (C to F) The lamella was cut and transferred onto a TEM half-grid, then fixed by Pt welding. (G) The lamella was then cut into 6 individual specimens, with further thinning process monitored by top-view imaging (H). (I) The individual specimens were consequently sculpted into T-shaped bridge tensile samples.

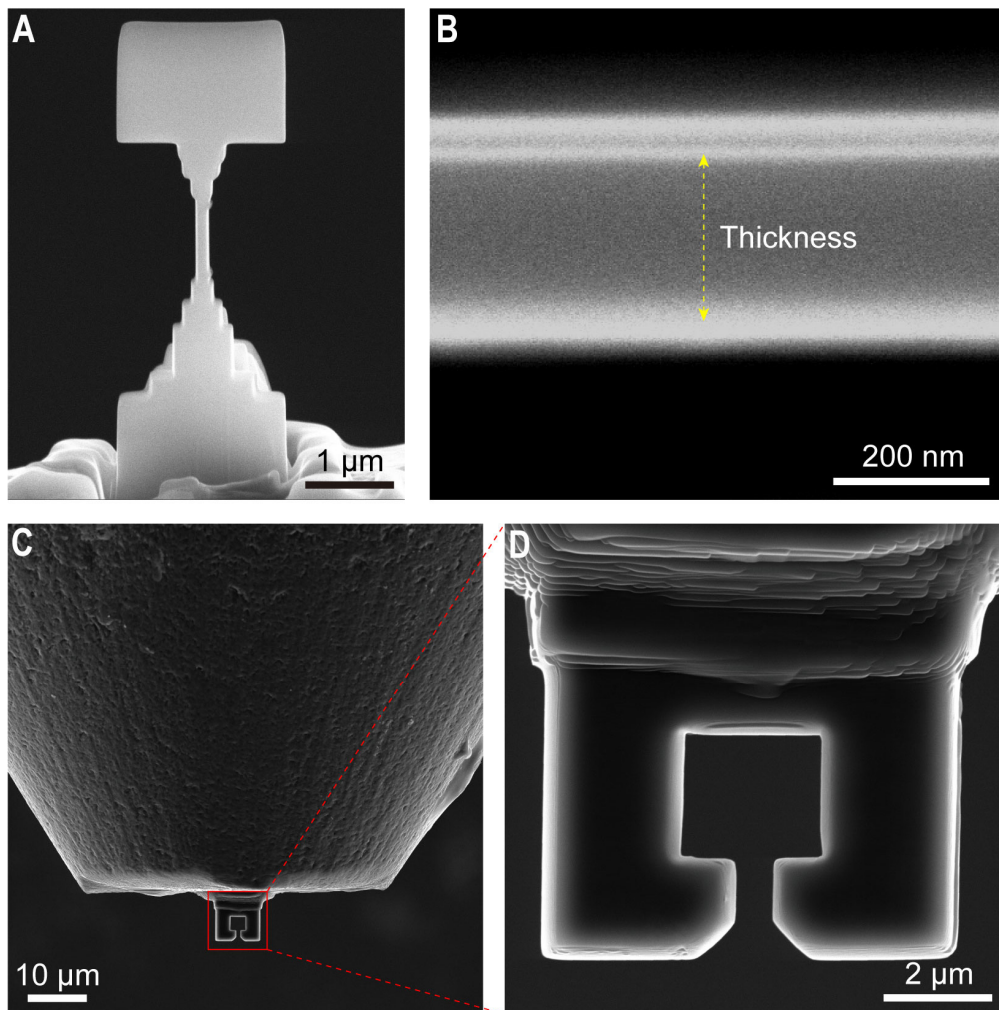


**Fig. S2.**

**SEM characterization of a diamond bridge sample and the diamond tensile gripper.** Side-view (A) and top-view (B) SEM images showing the FIB-sculpted diamond bridge sample. (C and D) side-view SEM images showing a microfabricated diamond tensile gripper.

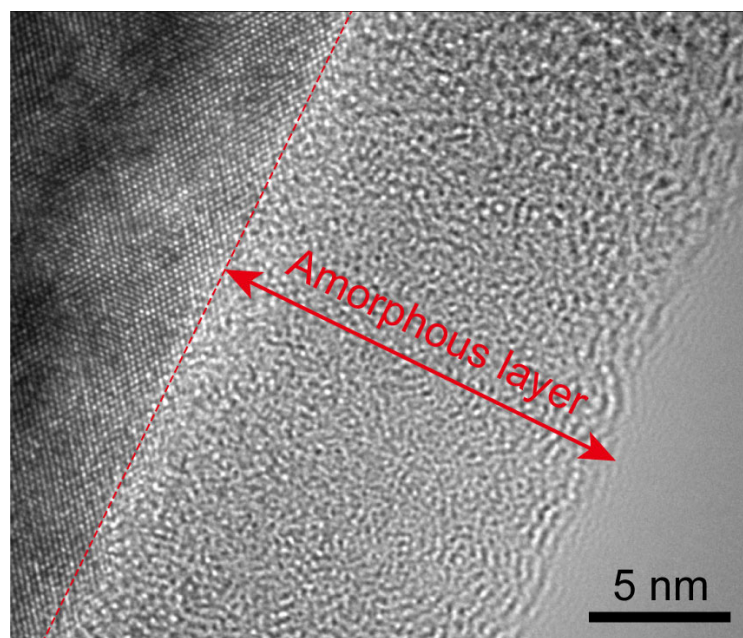


**Fig. S3.**

**Sample surface characterization.** A FIB-induced thin ( $\sim$ 15 nm thick) amorphous layer on the diamond bridge sample surface.

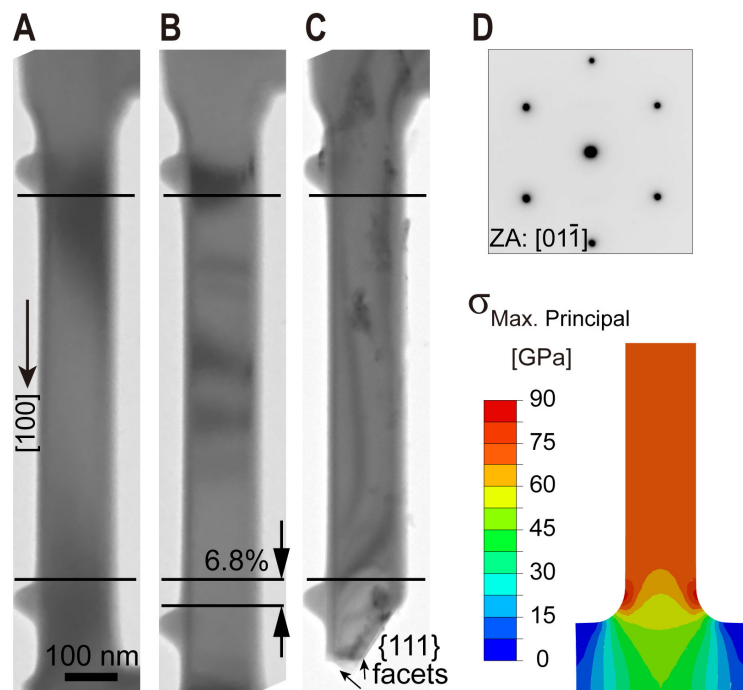


**Fig. S4.**

**in situ Tensile straining of a single-crystalline diamond bridge sample along the [100] direction.** (A to C) Extracted TEM image frames of the diamond bridge with the original state and the maximum deformation state before and after fracture at a failure strain (FS) of  $\sim 6.8\%$ . (D) FEM simulation reproducing the critical geometry of the sample shown in (B) and showing the amplitude of maximum principal stress ( $\sigma_{\text{Max. Principal}}$ ) distribution. Inset: the  $[01\bar{1}]$  zone axis (ZA) SAED pattern depicting that the loading is parallel to the [100] direction.

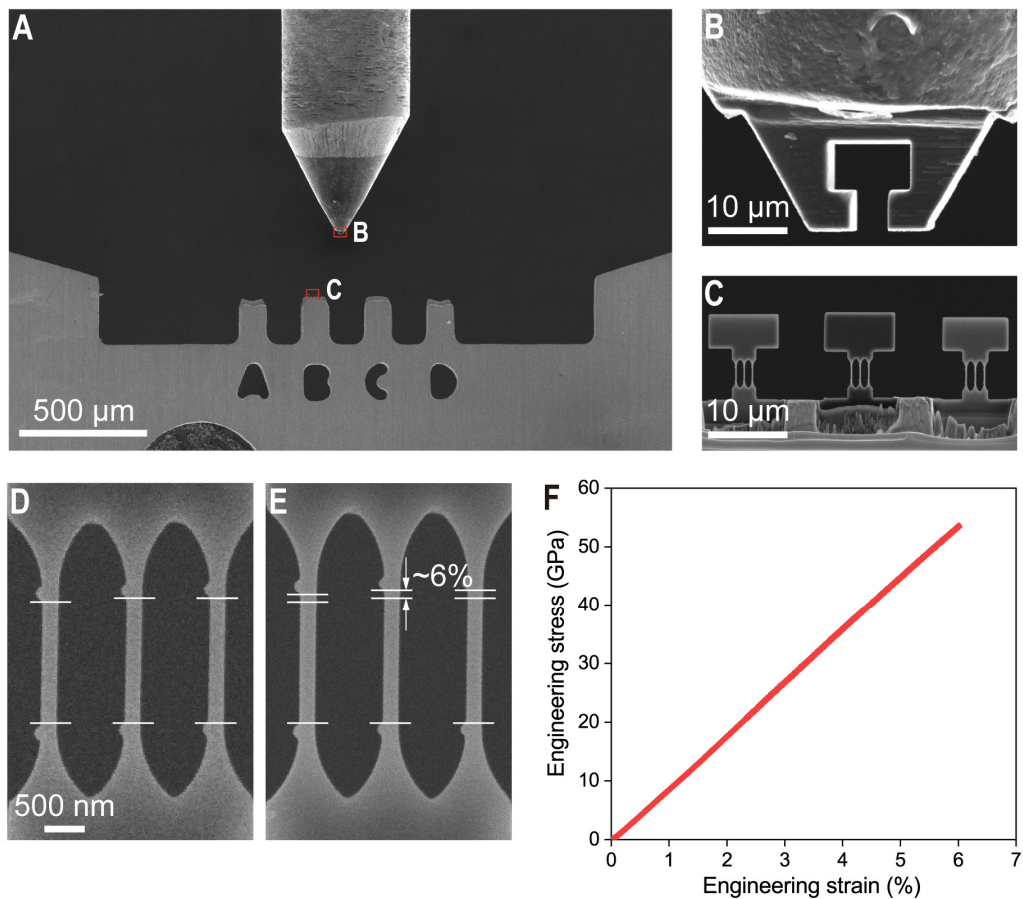


**Fig. S5.**

**in situ SEM tensile setup for straining diamond array samples.** (A) Overall view of the experimental setup and higher-magnification image depicting the (B) tensile gripper and the (C) diamond array samples. (D and E) Extracted SEM image frames of the [101]-oriented diamond array showing the maximum tensile strain of ~6% before fracture. The scale bars in (D and E) represent 500 nm. (F) Corresponding engineering stress-versus-strain curve of the tensile test.

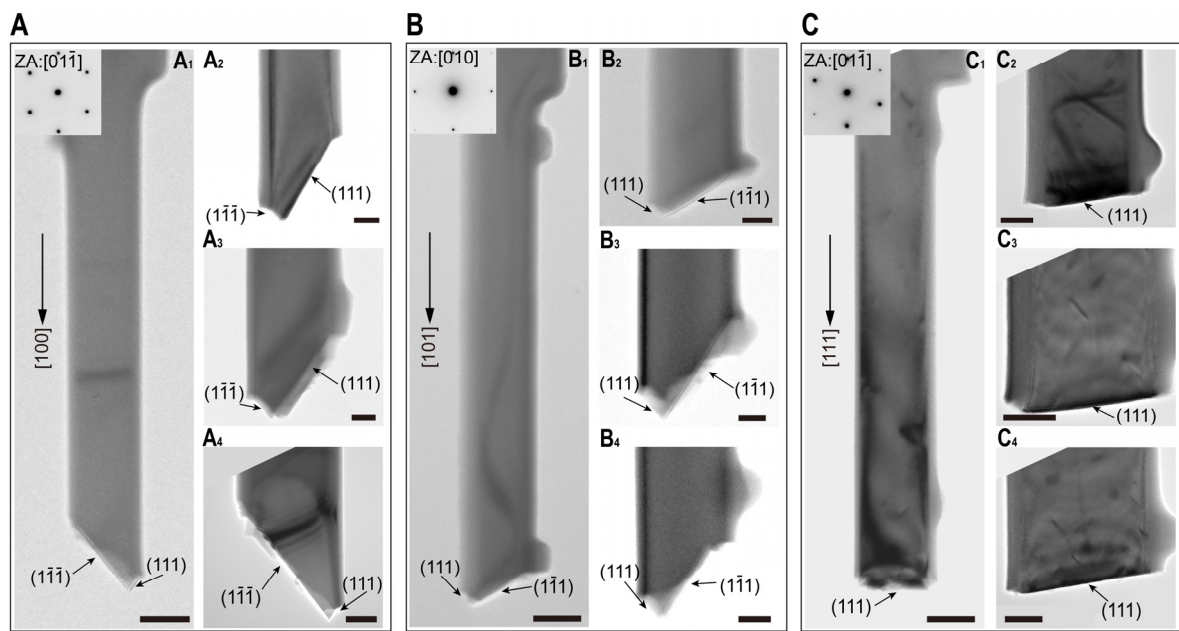


**Fig. S6.**

**Typical fracture morphologies of diamond bridges along [100], [101] and [111] directions.** (A to C) Bright-field TEM images showing typical brittle fracture morphologies, in which the diamonds remain mostly in the single-crystalline structure indicated by the inserted corresponding SAED patterns (A, B and C). Scale bars in A<sub>1</sub>, B<sub>1</sub> and C<sub>1</sub> represent 100 nm, and in A<sub>2</sub> to A<sub>4</sub>, B<sub>2</sub> to B<sub>4</sub>, C<sub>2</sub> to C<sub>4</sub> represent 50 nm, respectively.

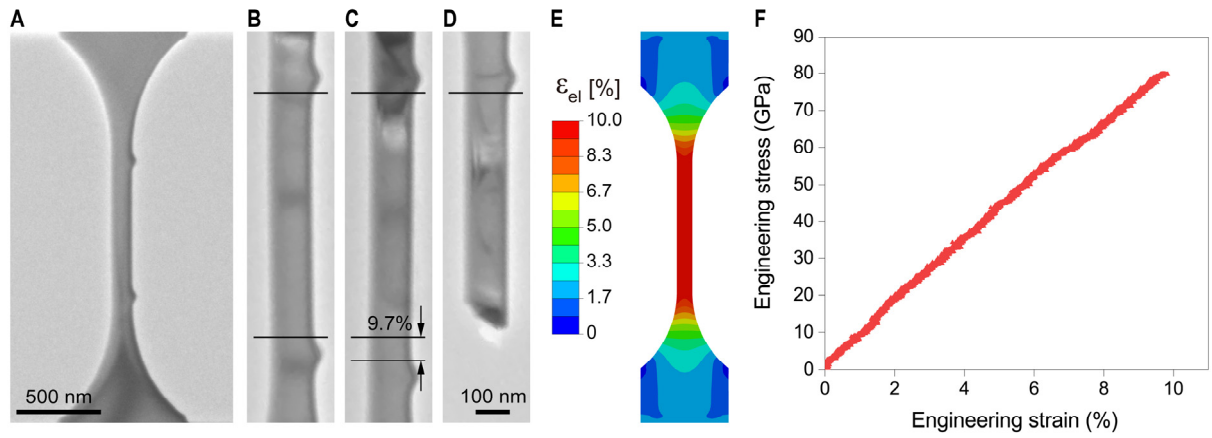


**Fig. S7.**

**in situ Tensile straining of the single-crystalline diamond bridge showing a maximum strain of ~9.7%.** (A) TEM image showing the optimized sample geometry. (B to D) Extracted TEM image frames of the diamond bridge with the original state and maximum deformation state at a tensile strain of ~9.7% before fracture. The scale bars in (B to D) represent 100 nm. (E) FEM simulation reproducing the critical geometry (front view) of the diamond bridge sample in (C) and showing the elastic strain ( $\epsilon_{el}$ ) distribution along the longitudinal direction. (F) Corresponding engineering stress-versus-strain curve.

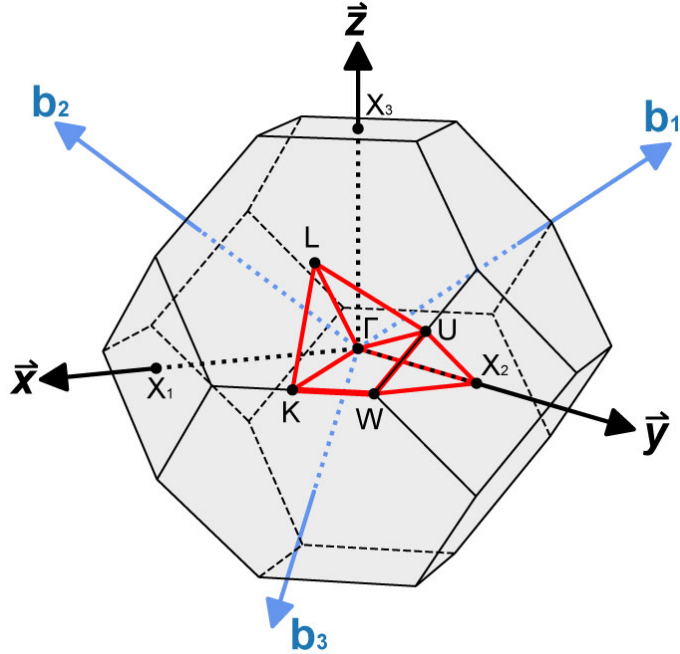


**Fig. S8.**

**Brillouin zone of diamond primitive cell without strain.** The three real lattice vectors are  $\vec{x}$ ,  $\vec{y}$  and  $\vec{z}$ . The corresponding reciprocal lattice vectors are  $\mathbf{b}_1$ ,  $\mathbf{b}_2$  and  $\mathbf{b}_3$ , and the marked points (black dots) are high-symmetry points. For clarity, we separately label the X points on the square faces along three lattice vectors as  $X_1$ ,  $X_2$  and  $X_3$ , which are parallel to  $2/a[100]$ ,  $2/a[010]$  and  $2/a[001]$  in reciprocal space, respectively, where  $a$  is the lattice constant of diamond cubic cell. We engage the band structure calculations through a subset of the original high-symmetry points as  $\Gamma-X_2-U-W-K-\Gamma-L-W-X_2$ . See also Movie S4.

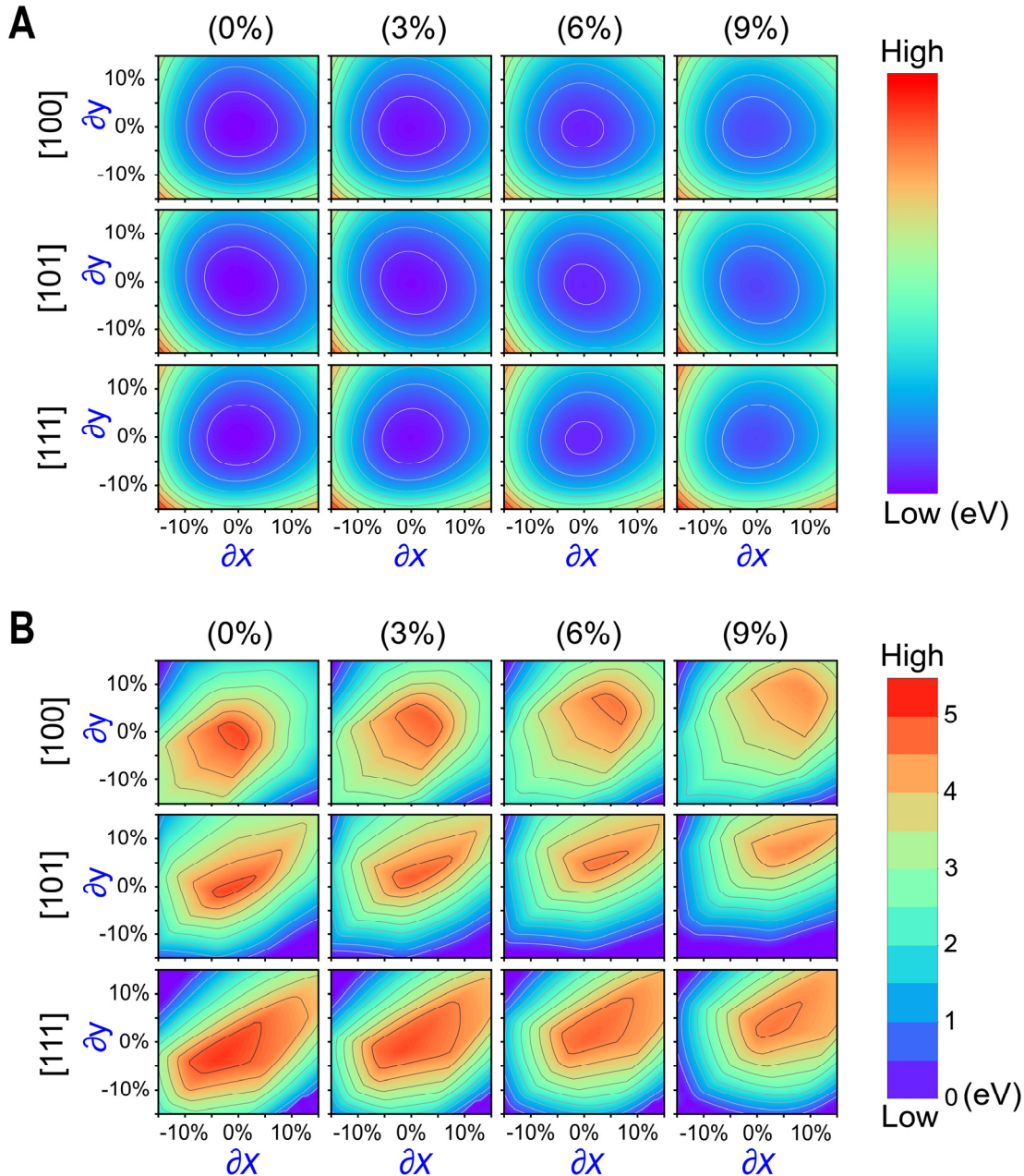


**Fig. S9.**

**The isosurface plots of calculated energy (A) and bandgap (B) for the [100]-, [101]- and [111]-oriented diamonds.** For each panel, the strain applies on  $z$ -axis (0%, 3%, 6% and 9%), and small perturbations  $\partial x$  and  $\partial y$  apply on  $x$ -axis and  $y$ -axis, respectively. In the energy plots, the lowest energy points are generally in the center of panel, only 1%  $x$ -axis shift is found for 9% strain along [111] direction. The results reveal that diamond has small Poisson contraction and barely has transverse change on non-loaded axis.

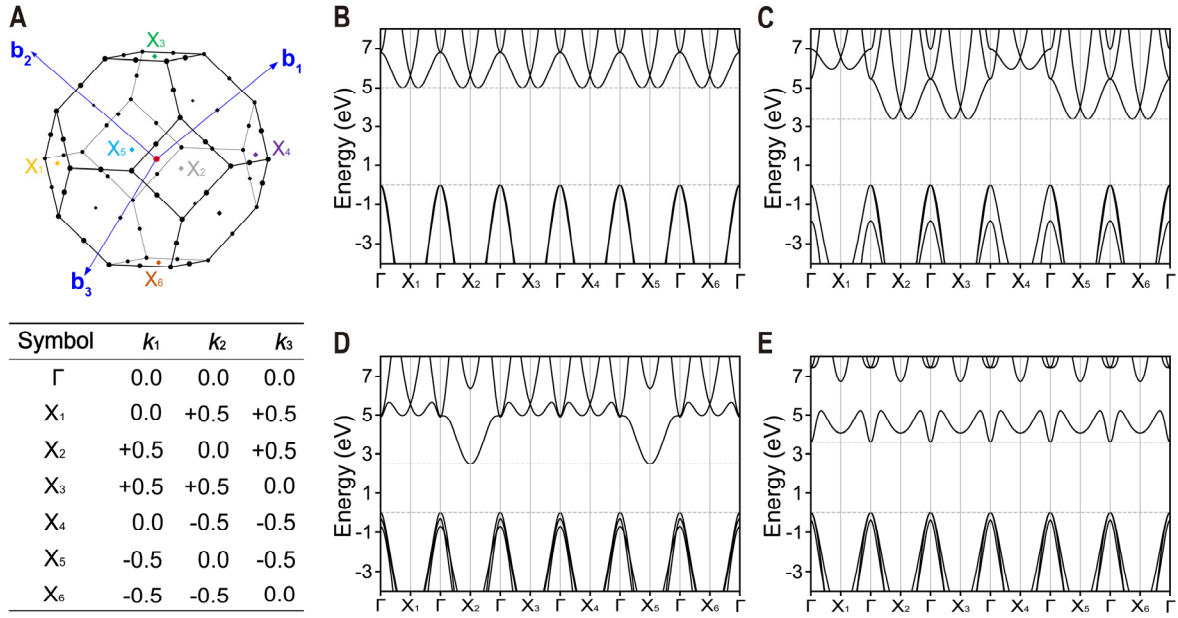


**Fig. S10.**

**Symmetry variations of the diamond Brillouin zone.** **(A)** Brillouin zone of ideal diamond and the positions of k-point  $\Gamma$ ,  $X_1$ ,  $X_2$ ,  $X_3$ ,  $X_4$ ,  $X_5$  and  $X_6$ . Band structures of **(B)** ideal diamond, **(C)** 12% strained [100]-oriented diamond, **(D)** 12% strained [101]-oriented diamond and **(E)** 12% strained [111]-oriented diamond.

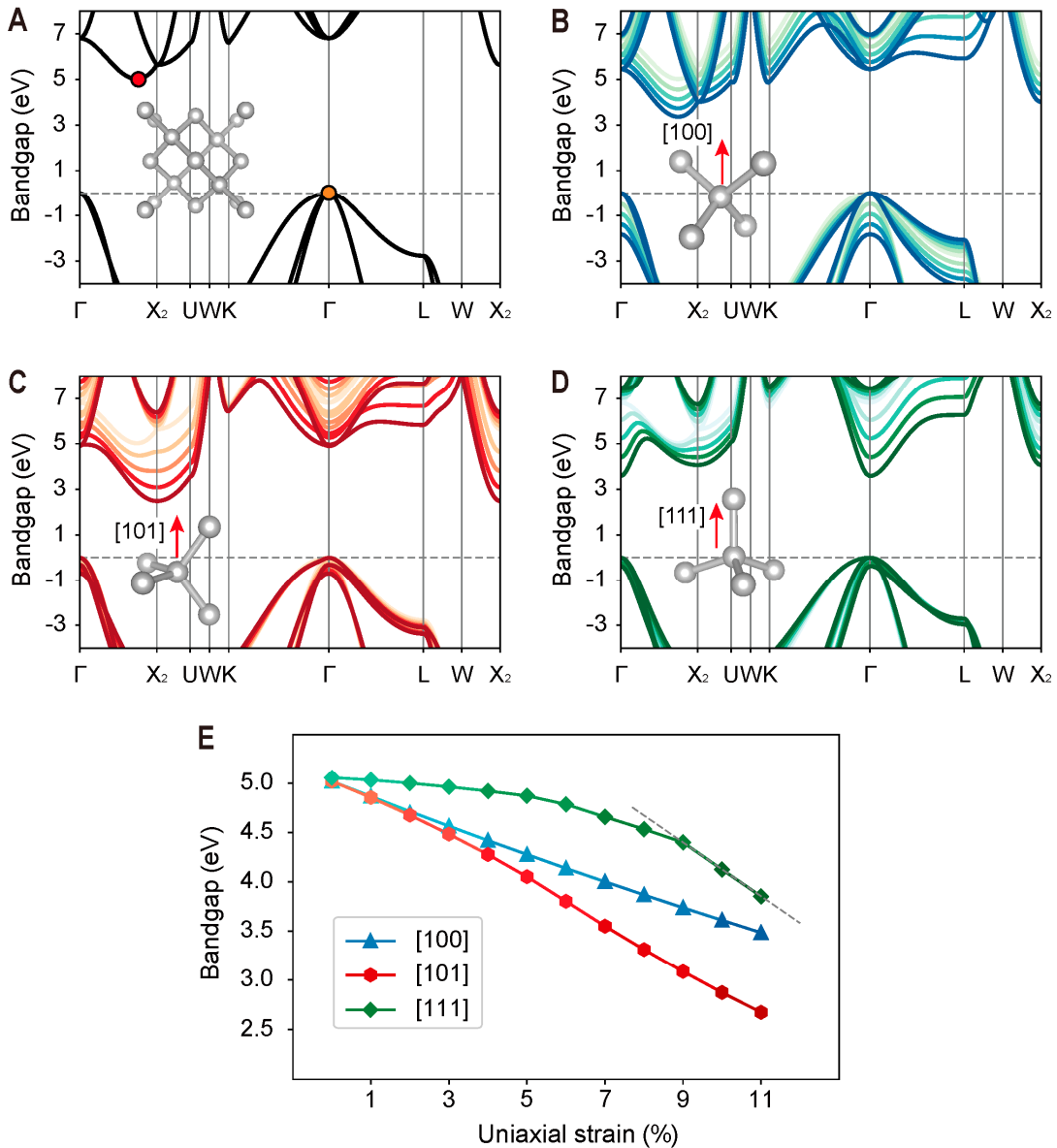


**Fig. S11.**

**Calculated diamond band structures** (A) The band structure of primitive diamond without strains. (B to D) The band structures under different tensile strains along [100], [101] and [111] directions, respectively. The k-path is selected as  $\Gamma$ - $X_2$ -U-W-K- $\Gamma$ -L-W- $X_2$ , the Brillouin zone is shown in Fig. S8 and the detailed information of high-symmetry points is listed in Table S1. Five lines with different color shades in (B to D) represent 0%, 3%, 6%, 9% and 12% strains, which the darker color stands for larger strain. All the band structures are aligned to the Fermi level. (E) The relationship of uniaxial strain and calculated bandgap values along [100], [101] and [111] directions. Indirect-to-direct bandgap transition occurs around ~9% tensile strain along the [111] direction.

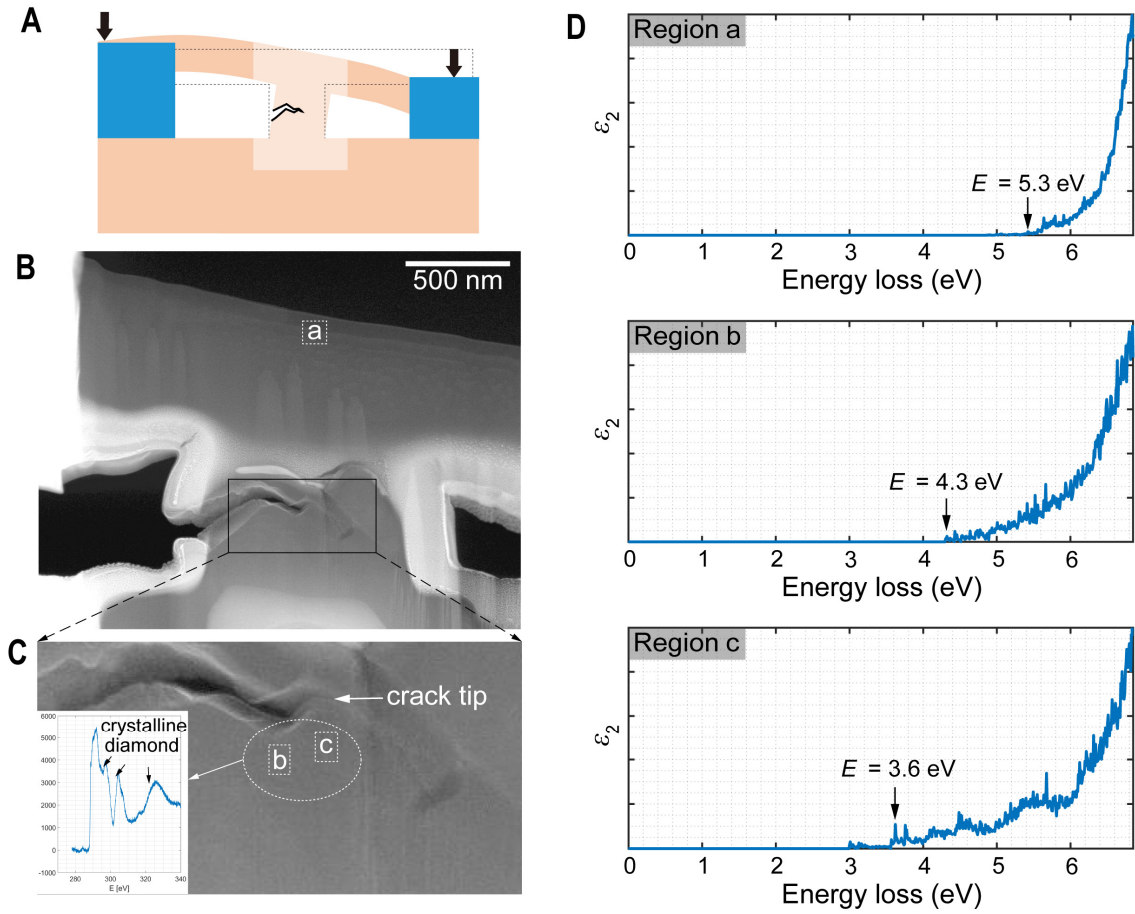


**Fig. S12.**

**Characterization of electronic bandgap in a pre-strained diamond sample by monochromated EELS.** (A) Schematic diagram of the pre-strained T-shaped diamond sample with both sides fixed and a bending crack forming in the middle. (B) STEM image of the pre-strained diamond sample with a bending crack in the center. (C) High-magnification STEM image of the crack area enlarged from the rectangular region in (B). Inset: core loss spectrum collected from the region of (b) and (c), confirming the crystalline diamond structure. (D) EELS low loss signal showing the bandgap measurements at the nearly strain-free region (a) and near the crack tip regions (b) and (c), respectively, where (c) is closer to the crack tip with a higher local strain.

**Table S1.****The k-point coordinates of primitive cell in band structure calculations (in scaled units)**

k-path: $\Gamma$ -X <sub>2</sub> -U-W-K- $\Gamma$ -L-W-X <sub>2</sub>			
symbol	$k_1$	$k_2$	$k_3$
$\Gamma$	0.000	0.000	0.000
X <sub>2</sub>	0.500	0.000	0.500
U	0.625	0.250	0.625
W	0.500	0.250	0.750
K	0.375	0.375	0.750
L	0.500	0.500	0.500

## **Supplementary Movie Captions**

### **Movie S1.**

in situ TEM movie showing three loading-unloading cycles of a single-crystalline diamond bridge sample along [101] direction (Fig. 2A-E), with fully recoverable deformation (played at 30 $\times$  speed).

### **Movie S2.**

in situ TEM movie showing the tensile test (Fig. S4A-C) of a single-crystalline diamond bridge sample along [100] direction (20 $\times$  speed).

### **Movie S3.**

in situ SEM movie showing the loading-unloading cycle of a [101]-oriented diamond array sample (Fig. 2I-J) with fully recoverable deformation (50 $\times$  speed).

### **Movie S4.**

Summary of the DFT calculations (including geometric structure, Brillouin zone, and band structure) of diamond with uniaxial strains in the range of 0-12% along [100], [101] and [111] directions, respectively.

## References and Notes

1. P. W. May, Materials science. The new diamond age? *Science* **319**, 1490–1491 (2008).  
[doi:10.1126/science.1154949](https://doi.org/10.1126/science.1154949) [Medline](#)
2. C. J. H. Wort, R. S. Balmer, Diamond as an electronic material. *Mater. Today* **11**, 22–28 (2008). [doi:10.1016/S1369-7021\(07\)70349-8](https://doi.org/10.1016/S1369-7021(07)70349-8)
3. I. Aharonovich, A. D. Greentree, S. Prawer, Diamond photonics. *Nat. Photonics* **5**, 397–405 (2011). [doi:10.1038/nphoton.2011.54](https://doi.org/10.1038/nphoton.2011.54)
4. J. E. Field, *The Properties of Natural and Synthetic Diamond* (Academic, 1992).
5. J. Isberg, J. Hammersberg, E. Johansson, T. Wikström, D. J. Twitchen, A. J. Whitehead, S. E. Coe, G. A. Scarsbrook, High carrier mobility in single-crystal plasma-deposited diamond. *Science* **297**, 1670–1672 (2002). [doi:10.1126/science.1074374](https://doi.org/10.1126/science.1074374) [Medline](#)
6. H. Watanabe, C. E. Nebel, S. Shikata, Isotopic homojunction band engineering from diamond. *Science* **324**, 1425–1428 (2009). [doi:10.1126/science.1172419](https://doi.org/10.1126/science.1172419) [Medline](#)
7. J. Y. Tsao, S. Chowdhury, M. A. Hollis, D. Jena, N. M. Johnson, K. A. Jones, R. J. Kaplar, S. Rajan, C. G. Van de Walle, E. Bellotti, C. L. Chua, R. Collazo, M. E. Coltrin, J. A. Cooper, K. R. Evans, S. Graham, T. A. Grotjohn, E. R. Heller, M. Higashiwaki, M. S. Islam, P. W. Juodawlkis, M. A. Khan, A. D. Koehler, J. H. Leach, U. K. Mishra, R. J. Nemanich, R. C. N. Pilawa-Podgurski, J. B. Shealy, Z. Sitar, M. J. Tadjer, A. F. Witulski, M. Wraback, J. A. Simmons, Ultrawide-bandgap semiconductors: Research opportunities and challenges. *Adv. Electron. Mater.* **4**, 1600501 (2018). [doi:10.1002/aelm.201600501](https://doi.org/10.1002/aelm.201600501)
8. K. Okano, S. Koizumi, S. R. P. Silva, G. A. J. Amaralunga, Low-threshold cold cathodes made of nitrogen-doped chemical-vapour-deposited diamond. *Nature* **381**, 140–141 (1996). [doi:10.1038/381140a0](https://doi.org/10.1038/381140a0)
9. R. Kalish, The search for donors in diamond. *Diam. Relat. Mater.* **10**, 1749–1755 (2001).  
[doi:10.1016/S0925-9635\(01\)00426-5](https://doi.org/10.1016/S0925-9635(01)00426-5)
10. Z. Teukam, J. Chevallier, C. Saguy, R. Kalish, D. Balltaud, M. Barbé, F. Jomard, A. Tromson-Carli, C. Cytermann, J. E. Butler, M. Bernard, C. Baron, A. Deneuville, Shallow donors with high n-type electrical conductivity in homoepitaxial deuterated boron-doped diamond layers. *Nat. Mater.* **2**, 482–486 (2003). [doi:10.1038/nmat929](https://doi.org/10.1038/nmat929) [Medline](#)
11. J. J. Gilman, *Electronic Basis of the Strength of Materials* (Cambridge Univ. Press, 2003).
12. T. Zhu, J. Li, Ultra-strength materials. *Prog. Mater. Sci.* **55**, 710–757 (2010).  
[doi:10.1016/j.pmatsci.2010.04.001](https://doi.org/10.1016/j.pmatsci.2010.04.001)
13. J. Li, Z. Shan, E. Ma, Elastic strain engineering for unprecedented materials properties. *MRS Bull.* **39**, 108–114 (2014). [doi:10.1557/mrs.2014.3](https://doi.org/10.1557/mrs.2014.3)
14. A. Banerjee, D. Bernoulli, H. Zhang, M.-F. Yuen, J. Liu, J. Dong, F. Ding, J. Lu, M. Dao, W. Zhang, Y. Lu, S. Suresh, Ultralarge elastic deformation of nanoscale diamond. *Science* **360**, 300–302 (2018). [doi:10.1126/science.aar4165](https://doi.org/10.1126/science.aar4165) [Medline](#)

15. A. Nie, Y. Bu, P. Li, Y. Zhang, T. Jin, J. Liu, Z. Su, Y. Wang, J. He, Z. Liu, H. Wang, Y. Tian, W. Yang, Approaching diamond's theoretical elasticity and strength limits. *Nat. Commun.* **10**, 5533 (2019). [doi:10.1038/s41467-019-13378-w](https://doi.org/10.1038/s41467-019-13378-w) Medline
16. D. Roundy, M. L. Cohen, Ideal strength of diamond, Si, and Ge. *Phys. Rev. B* **64**, 212103 (2001). [doi:10.1103/PhysRevB.64.212103](https://doi.org/10.1103/PhysRevB.64.212103)
17. J. M. Wheeler, R. Raghavan, J. Wehrs, Y. Zhang, R. Erni, J. Michler, Approaching the limits of strength: Measuring the uniaxial compressive strength of diamond at small scales. *Nano Lett.* **16**, 812–816 (2016). [doi:10.1021/acs.nanolett.5b04989](https://doi.org/10.1021/acs.nanolett.5b04989) Medline
18. Z. Shi, E. Tsymbalov, M. Dao, S. Suresh, A. Shapeev, J. Li, Deep elastic strain engineering of bandgap through machine learning. *Proc. Natl. Acad. Sci. U.S.A.* **116**, 4117–4122 (2019). [doi:10.1073/pnas.1818555116](https://doi.org/10.1073/pnas.1818555116) Medline
19. C. Liu, X. Song, Q. Li, Y. Ma, C. Chen, Smooth flow in diamond: Atomistic ductility and electronic conductivity. *Phys. Rev. Lett.* **123**, 195504 (2019). [doi:10.1103/PhysRevLett.123.195504](https://doi.org/10.1103/PhysRevLett.123.195504) Medline
20. H. Zhang, J. Tersoff, S. Xu, H. Chen, Q. Zhang, K. Zhang, Y. Yang, C.-S. Lee, K.-N. Tu, J. Li, Y. Lu, Approaching the ideal elastic strain limit in silicon nanowires. *Sci. Adv.* **2**, e1501382 (2016). [doi:10.1126/sciadv.1501382](https://doi.org/10.1126/sciadv.1501382) Medline
21. G. Shu, B. Dai, V. G. Ralchenko, A. P. Bolshakov, A. A. Khomich, E. E. Ashkinazi, J. Han, J. Zhu, Growth of three-dimensional diamond mosaics by microwave plasma-assisted chemical vapor deposition. *CrystEngComm* **20**, 198–203 (2018). [doi:10.1039/C7CE01706E](https://doi.org/10.1039/C7CE01706E)
22. G. Shu, B. Dai, V. G. Ralchenko, A. P. Bolshakov, A. A. Khomich, E. E. Ashkinazi, V. Y. Yurov, K. Yao, K. Liu, J. Zhao, J. Han, J. Zhu, Vertical-substrate epitaxial growth of single-crystal diamond by microwave plasma-assisted chemical vapor deposition. *J. Cryst. Growth* **486**, 104–110 (2018). [doi:10.1016/j.jcrysgro.2018.01.024](https://doi.org/10.1016/j.jcrysgro.2018.01.024)
23. D. Kiener, A. M. Minor, Source truncation and exhaustion: Insights from quantitative in situ TEM tensile testing. *Nano Lett.* **11**, 3816–3820 (2011). [doi:10.1021/nl201890s](https://doi.org/10.1021/nl201890s) Medline
24. W. Kohn, L. J. Sham, Self-consistent equations including exchange and correlation effects. *Phys. Rev.* **140** (4A), A1133–A1138 (1965). [doi:10.1103/PhysRev.140.A1133](https://doi.org/10.1103/PhysRev.140.A1133)
25. Materials and methods are available as supplementary materials.
26. R. H. Telling, C. J. Pickard, M. C. Payne, J. E. Field, Theoretical strength and cleavage of diamond. *Phys. Rev. Lett.* **84**, 5160–5163 (2000). [doi:10.1103/PhysRevLett.84.5160](https://doi.org/10.1103/PhysRevLett.84.5160) Medline
27. J. E. Field, The mechanical and strength properties of diamond. *Rep. Prog. Phys.* **75**, 126505 (2012). [doi:10.1088/0034-4885/75/12/126505](https://doi.org/10.1088/0034-4885/75/12/126505) Medline
28. ASTM Standard C1273-18, "Standard Test Method for Tensile Strength of Monolithic Advanced Ceramics at Ambient Temperatures" (ASTM International, 2018); <https://doi.org/10.1520/C1273-18>.

29. P. Ovartchaiyapong, K. W. Lee, B. A. Myers, A. C. B. Jayich, Dynamic strain-mediated coupling of a single diamond spin to a mechanical resonator. *Nat. Commun.* **5**, 4429 (2014). [doi:10.1038/ncomms5429](https://doi.org/10.1038/ncomms5429) [Medline](#)
30. B. Khanaliloo, H. Jayakumar, A. C. Hryciw, D. P. Lake, H. Kaviani, P. E. Barclay, Single-crystal diamond nanobeam waveguide optomechanics. *Phys. Rev. X* **5**, 041051 (2015). [doi:10.1103/PhysRevX.5.041051](https://doi.org/10.1103/PhysRevX.5.041051)
31. J. J. Hamlin, B. B. Zhou, Extreme diamond-based quantum sensors. *Science* **366**, 1312–1313 (2019). [doi:10.1126/science.aaz4982](https://doi.org/10.1126/science.aaz4982) [Medline](#)
32. Dassault Systèmes Simulia, *ABAQUS 6.14 Theory Guide, Section 4.6.1, Hyperelastic Material Behavior* (Dassault Systèmes, 2014).
33. G. Kresse, J. Furthmüller, Efficiency of ab-initio total energy calculations for metals and semiconductors using a plane-wave basis set. *Comput. Mater. Sci.* **6**, 15–50 (1996). [doi:10.1016/0927-0256\(96\)00008-0](https://doi.org/10.1016/0927-0256(96)00008-0)
34. G. Kresse, J. Furthmüller, Efficient iterative schemes for ab initio total-energy calculations using a plane-wave basis set. *Phys. Rev. B* **54**, 11169–11186 (1996). [doi:10.1103/PhysRevB.54.11169](https://doi.org/10.1103/PhysRevB.54.11169) [Medline](#)
35. P. E. Blöchl, O. Jepsen, O. K. Andersen, Improved tetrahedron method for Brillouin-zone integrations. *Phys. Rev. B* **49**, 16223–16233 (1994). [doi:10.1103/PhysRevB.49.16223](https://doi.org/10.1103/PhysRevB.49.16223) [Medline](#)
36. M. P. Surh, S. G. Louie, M. L. Cohen, Band gaps of diamond under anisotropic stress. *Phys. Rev. B* **45**, 8239–8247 (1992). [doi:10.1103/PhysRevB.45.8239](https://doi.org/10.1103/PhysRevB.45.8239) [Medline](#)
37. J. P. Perdew, K. Burke, M. Ernzerhof, Generalized gradient approximation made simple. *Phys. Rev. Lett.* **77**, 3865–3868 (1996). [doi:10.1103/PhysRevLett.77.3865](https://doi.org/10.1103/PhysRevLett.77.3865) [Medline](#)
38. J. Sun, B. Xiao, A. Ruzsinszky, Communication: Effect of the orbital-overlap dependence in the meta generalized gradient approximation. *J. Chem. Phys.* **137**, 051101 (2012). [doi:10.1063/1.4742312](https://doi.org/10.1063/1.4742312) [Medline](#)
39. J. Sun, R. Haunschild, B. Xiao, I. W. Bulik, G. E. Scuseria, J. P. Perdew, Semilocal and hybrid meta-generalized gradient approximations based on the understanding of the kinetic-energy-density dependence. *J. Chem. Phys.* **138**, 044113 (2013). [doi:10.1063/1.4789414](https://doi.org/10.1063/1.4789414) [Medline](#)
40. P. Hess, The mechanical properties of various chemical vapor deposition diamond structures compared to the ideal single crystal. *J. Appl. Phys.* **111**, 051101 (2012). [doi:10.1063/1.3683544](https://doi.org/10.1063/1.3683544)
41. H. Hirai, M. Terauchi, M. Tanaka, K. Kondo, Estimating band gap of amorphous diamond and nanocrystalline diamond powder by electron energy loss spectroscopy. *Diamond Related Materials* **8**, 1703–1706 (1999). [doi:10.1016/S0925-9635\(99\)00045-X](https://doi.org/10.1016/S0925-9635(99)00045-X)
42. A. Nie, Y. Bu, J. Huang, Y. Shao, Y. Zhang, W. Hu, J. Liu, Y. Wang, B. Xu, Z. Liu, H. Wang, W. Yang, Y. Tian, Direct observation of room-temperature dislocation plasticity in diamond. *Matter* **2**, 1222–1232 (2020). [doi:10.1016/j.matt.2020.02.011](https://doi.org/10.1016/j.matt.2020.02.011)

43. B. A. Fairchild, S. Rubanov, D. W. M. Lau, M. Robinson, I. Suarez-Martinez, N. Marks, A. D. Greentree, D. McCulloch, S. Prawer, Mechanism for the amorphisation of diamond. *Adv. Mater.* **24**, 2024–2029 (2012). [doi:10.1002/adma.201104511](https://doi.org/10.1002/adma.201104511) [Medline](#)
44. B. Lawn, *Fracture of Brittle Solids* (Cambridge Univ. Press, ed. 2, 1993).
45. D. F. Blake, F. Freund, K. F. M. Krishnan, C. J. Echer, R. Shipp, T. E. Bunch, A. G. Tielens, R. J. Lipari, C. J. D. Hetherington, S. Chang, The nature and origin of interstellar diamond. *Nature* **332**, 611–613 (1988). [doi:10.1038/332611a0](https://doi.org/10.1038/332611a0) [Medline](#)
46. R. F. Egerton, *Electron Energy-Loss Spectroscopy in the Electron Microscope* (Springer, 2011).
47. L. Zhang, R. Erni, J. Verbeeck, G. Van Tendeloo, Retrieving the dielectric function of diamond from valence electron energy-loss spectroscopy. *Phys. Rev. B* **77**, 195119 (2008). [doi:10.1103/PhysRevB.77.195119](https://doi.org/10.1103/PhysRevB.77.195119)